Vrije Universiteit Brussel

# Scaling laws for robotic transmissions

Saerens, Elias; Crispel, Stein; Lopez Garcia, Pablo; Verstraten, Tom; Ducastel, Vincent; Vanderborght, Bram; Lefeber, Dirk

*Published in:*
Mechanism and Machine Theory

*DOI:*
10.1016/j.mechmachtheory.2019.06.027

*Publication date:*
2019

*Document Version:*
Submitted manuscript

Link to publication

*Citation for published version (APA):*
Saerens, E., Crispel, S., Lopez Garcia, P., Verstraten, T., Ducastel, V., Vanderborght, B., & Lefeber, D. (2019). Scaling laws for robotic transmissions. *Mechanism and Machine Theory*, *140*(October 2019), 601-621. https://doi.org/10.1016/j.mechmachtheory.2019.06.027

**Copyright**
No part of this publication may be reproduced or transmitted in any form, without the prior written permission of the author(s) or other rights holders to whom publication rights have been transferred, unless permitted by a license attached to the publication (a Creative Commons license or other), or unless exceptions to copyright law apply.

**Take down policy**
If you believe that this document infringes your copyright or other rights, please contact openaccess@vub.be, with details of the nature of the infringement. We will investigate the claim and if justified, we will take the appropriate steps.

Download date: 09. Apr. 2024

ResearchGate

See discussions, stats, and author profiles for this publication at: https://www.researchgate.net/publication/334030874

# Scaling laws for robotic transmissions

**Article** *in* Mechanism and Machine Theory · October 2019

DOI: 10.1016/j.mechmachtheory.2019.06.027

CITATIONS
0

READS
164

**7 authors**, including:

Elias Saerens
Vrije Universiteit Brussel

**10** PUBLICATIONS **2** CITATIONS

SEE PROFILE

Stein Crispel
Vrije Universiteit Brussel

**10** PUBLICATIONS **2** CITATIONS

SEE PROFILE

Pablo Lopez Garcia
Vrije Universiteit Brussel

**11** PUBLICATIONS **14** CITATIONS

SEE PROFILE

Tom Verstraten
Vrije Universiteit Brussel

**38** PUBLICATIONS **181** CITATIONS

SEE PROFILE

**Some of the authors of this publication are also working on these related projects:**

Project ALTACRO View project

Project Pepper robot in a retail environment View project

All content following this page was uploaded by Elias Saerens on 26 June 2019.

The user has requested enhancement of the downloaded file.

# Scaling laws for robotic transmissions

Elias Saerens*, Stein Crispel, Pablo López García, Tom Verstraten, Vincent Ducastel, Bram Vanderborght and Dirk Lefeber

***Abstract*—In robotic actuators, low speeds and high torques are usually required. Small electric motors, which are more efficient at high speeds and low torques, do not fit the requirements directly. In order to transform the motor characteristics into the desired output characteristics, a transmission system is needed. Ideally, it should be optimally designed and adapted to the desired characteristics and the available space. Scaling laws can provide a way to design these desired output requirements as a function of the size parameters. These are however not yet available for transmission systems. To fill this gap, several scaling laws are developed throughout this paper for some of the most important robotic characteristics, i.e. maximum continuous output torque and reflected inertia, in function of the number of stages, the transmission ratio and the size parameters of different types of transmissions. These laws show that diameter has a much bigger influence on the characteristics of transmissions than length. All derived laws show good comparison with catalog data of manufacturers like Maxon, Moog, Neugart, Harmonic Drive®, Sumitomo and SKF.**

***Keywords*—scaling laws, planetary gearbox, harmonic drive, cycloid drive, ball screw**

## I. INTRODUCTION

In robotics, a new generation of actuators is needed to fulfill the demands of the future. These actuators should have characteristics such as high efficiency, high torque capacity, high power density, high energy density, low weight, etc. In terms of high energy density and power, hydraulic systems are superior [1]. They however induce rather large losses and often require external power sources, which makes the design more space consuming and heavier. As a result, their application potential is limited. In particular, these drawbacks are unacceptable for the evolving fields of mobile and wearable robots (e.g. exoskeletons), where efficiency and low mass are crucial [2].

To overcome these issues, nowadays mainly electric (especially BLDC, PMSM and PMAC) are used due to their favourable characteristics like high efficiency (when used in the correct operation range), high bandwidth, high positioning accuracy, etc. [3]. However, they lack a high torque density, due to the fact that limited electromagnetic forces can be produced at a small scale [4]. Because of this, transmission systems are coupled to the electric motor output in order to convert the high speed, low torque characteristics of the motor into the more favourable low speed, high torque, which is needed for robotic actuators. The influence of such transmissions is however often not well taken into account, which leads to a decrease of the overall energy efficiency [5], [6].

Since robotics is a field in which high performance normally needs to be combined with low weight and small volume, a multi-parameter optimization is needed. This optimization process can be facilitated using scaling laws.

Several works in literature already address the optimal selection of transmissions and especially how they influence the overall actuator.

Rezazadeh et al. [7] studied the efficiency of a geared motor, with a focus on improving the energy efficiency of the motor by selecting the optimal transmission ratio. By doing so, the motor can work in its optimal range. This selection is done analytically by considering a transmission that has a constant efficiency for each load case and considers for the motor only Joule losses.

Bartlett et al. [8] on the other hand, dug deeper into multiple-stage gearboxes. Here, an analysis is performed on how some design parameters, such as the number of stages and stage ratios, influence the total mechanical efficiency, mass and acceleration. This way, they aim to find the best trade-off between conflicting gearbox characteristics [9].

Considering scaling laws for transmissions, one of the few contributions was delivered by Pott [10], who derived how the torque and mechanical power of gearboxes scale as a function of a general dimensional unit ’s’. The downside of this method is that in such a way no distinction can be made between the effect of a diameter or length change, which can potentially be important for certain applications.

A more extensive derivation was done by Radzevich [11]. He described a so-called ’Q-factor’ that scales the weight of a spur gear pair or a planetary gear train for different load cases. This Q-factor is a function of the transmission ratio and power of the gearbox.

For scaling laws of almost each actuator component, and hence also transmissions, Budinger et al. [12] can be consulted. They provided among others the scaling laws for all the classic transmissions. Their derivations are however not explained in-depth, which makes it hard to verify the made assumptions. They use torque/force as main scaling parameter and only find a link with the outside dimensions through a component integrator perspective, due to this different aim it is more difficult to use this reference for volume-based scaling, which is crucial in robotics.

---

Robotics & Multibody Mechanics Research Group (R&MM), Department of Mechanical Engineering, Vrije Universiteit Brussel and Flanders Make, 1050 Brussels, Belgium.

* Corresponding Author: elias.saerens@vub.be (Elias Saerens)

Preprint submitted to Mechanism & Machine Theory

Many robots have two distinct operating modes:

1) Carrying the payload
2) Movement without payload

For the first, the maximum continuous output torque is often the limiting factor. For the second, the mass of the robotic arm and the inertial load of the actuators are the only load. This implies that a maximum achievable output torque and a minimal inertia are desired. However, often only limited space is available, especially in the fields of wearable robotics. This makes it interesting if the torque and inertia could be written in function of dimensional parameters.

Hence, in this paper, we will derive scaling laws for maximum continuous output torque and reflected inertia, for most transmissions: multi-stage parallel shaft and planetary gear trains, harmonic drives, cycloid drives and ball screws. This is especially important in dynamic robots or robots that experience intermittent contact with the environment. To enable direct comparison with the load inertia, we will calculate the reflected inertia from a load-side perspective.

To tackle the fact that none of the existing scaling laws are given as a function of size parameters, which is crucial for complex actuators that use multiple parallel motors and transmissions like e.g. the +SPEA [13] and DMA [14], the laws derived in this paper will be written as a function of the main design parameters of transmissions, i.e. outer diameter, outer length, number of stages and transmission ratio. The derivations of these laws will be done thoroughly. This in order to provide the reader a better insight in the failure mechanisms of each transmission and to show how these laws are constructed and which assumptions are made, which is different from the current literature.

The layout of the paper is as follows. First, in section II, derivations for the scaling laws of both maximum continuous output torque and total reflected inertia will be performed for different types of multi-stage gear trains (parallel shaft and planetary). These laws will then be compared to existing catalog data from gearbox-manufacturers like Maxon, Moog and Neugart. In section III, the same approach will be used to tackle the scaling of harmonic drives. There, the derived laws will be compared to the CSG and CSF series of Harmonic Drive®. This same procedure will be repeated in both section IV and V for respectively cycloid drives and ball screws. The found scaling laws for cycloid drives will be compared to catalog data from Sumitomo whereas data from SKF will be used to verify the found laws of ball screws. Afterwards, in section VI, an overview of the found laws will be given together with a comparison of the different transmission types based on catalog data. This comparison will be done among the different discussed transmissions for characteristics such as inertia vs. torque and torque vs mass. Furthermore, in this section, typical motor inertia will be compared with the inertia of the discussed transmissions. Finally, in section VII a conclusion will be given.

General design parameters, which will appear throughout the document, are summarized in Table I.

| Symbol | Explanation | Unit |
|---|---|---|
| $T_{in,max}$ | Maximum allowed continuous input torque | $Nm$ |
| $T_{out,max}$ | Maximum allowed continuous output torque | $Nm$ |
| $L$ | Outer length of the transmission | $m$ |
| $d$ | Outer diameter of the transmission | $m$ |
| $a$ | Number of transmission stages | / |
| $i$ | Transmission ratio ($=\frac{\omega_{in}}{\omega_{out}}$) | / |
| $m$ | Gear module | $m$ |
| $\sigma_{H,max}$ | Maximum Hertz/contact stress | $\frac{N}{m^2}$ |
| $\sigma_{H,ut}$ | Maximum allowable contact stress | $\frac{N}{m^2}$ |
| $\sigma_{F,max}$ | Maximum bending stress | $\frac{N}{m^2}$ |
| $\sigma_{F,ut}$ | Maximum allowable bending stress | $\frac{N}{m^2}$ |

TABLE I: Nomenclature of general transmission parameters.

## II. SCALING FOR MULTI-STAGE GEAR TRAINS

In this section, the scaling of multi-stage gear trains, i.e. parallel shaft gear trains (PSGT) and epicyclic or planetary gear trains (PGT), will be investigated.

Gear engineers normally use the earlier mentioned Q-factor [11] if sizing for weight is needed. However, when other parameters like torque are required, Pott [10] suggests to look at the maximal bending moment. This section will start from stress calculations, but will also include other types of stress, like contact stress. The results will then also be compared to catalog data from Maxon [15] for the parallel shaft gears and both maxon [15], Moog [16] and Neugart [17] for the planetary gears.

### A. Parallel Shaft Gear Train (PSGT)

In this subsection, calculations are made regarding parallel shaft gear trains. The parameters involved in the calculations of this subsection, which are specific to the PSGT, are summarized in Table II.

| Symbol | Explanation | Unit |
|---|---|---|
| $d_1$ | Pitch diameter of the Pinion | $m$ |
| $d_2$ | Pitch diameter of the Gear | $m$ |
| $\omega_1$ | Rotational speed of the Pinion | $m$ |
| $\omega_2$ | Rotational speed of the Gear | $m$ |
| $i_s$ | Transmission ratio in one stage ($=\frac{\omega_{in}}{\omega_{out}}=\frac{\omega_1}{\omega_2}$) | / |
| $J_{PSGT}$ | Mass moment of inertia of the parallel shaft gear train | $kgm^2$ |
| $b$ | Effective teeth width | $m$ |
| $b_s$ | Effective teeth width in one stage | $m$ |
| $b_f$ | Effective gear face | $m$ |

TABLE II: Nomenclature of PSGT specific parameters

There are also some empirical parameters involved in the gear calculations (for both parallel shaft and planetary gears). These are summarized in Table III.

Here, derivations are initially done for one stage and only later expanded to multi-stage gearboxes. The lay-out of such kind of gearboxes can be seen in Fig. 1. Hence, when the calculations are only valid in one stage, the subscript ”$s$” will be used to denote this.

Here, only parallel shaft gear trains with a cylindrical casing will be investigated. This is done since these are the ones that are most usefull in robotic transmissions.

| Symbol | Explanation | Unit |
|---|---|---|
| $K_H$ | Gear contact load factor | / |
| $K_F$ | Gear bending load factor | / |
| $Y_{FS}$ | Shape and stress concentration factor | / |
| $Y_\beta$ | Tooth tilt angle factor | / |
| $Y_\varepsilon$ | Teeth overlap factor | / |
| $Z_E$ | Material parameter factor | / |
| $Z_H$ | Gear teeth shape factor | / |
| $Z_\varepsilon$ | Contact line correction factor | / |

TABLE III: Nomenclature of empirical gear design parameters

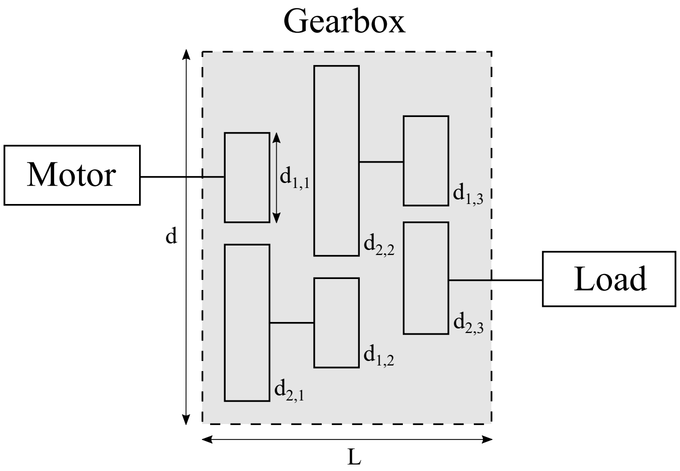

Fig. 1: Overview of the structure of a multi-stage parallel shaft gear train (PSGT) (here the number of stages $a = 3$). The dashed lines represent the housing of the gearbox. Here the notation $d_{i,j}$ is used, where $i$ indicates if it is the Pinion (1) or Gear (2) and $j$ denotes the stage number.

It should also be noted that in this subsection, the subscript 1 will refer to the Pinion and 2 to the Gear.

### 1) Maximum Torque:

One of the key factors in gear design are the stresses inside the gears. In PSGTs there are two types of stresses that can occur, namely contact or Hertz stress ($\sigma_H$), which occurs at the contact points (the tip) and bending stress ($\sigma_F$), which occurs at the root of the teeth.

According to [18] the maximum stresses, for respectively contact and bending in gears, are given by:

$$\begin{cases} \sigma_{H,max} = Z_E Z_H Z_\varepsilon \sqrt{\frac{2000 K_H T_{in}(i_s \pm 1)}{d_1^2 b_f i_s}} \\ \\ \sigma_{F,max} = \frac{2000 K_F T_{in} Y_{FS} Y_\beta Y_\varepsilon}{d_1 b m} \end{cases} \tag{1}$$

Here a "$\pm$" is used, since the sign changes depending on the gearing used. For external gears a "$+$" is adopted, whereas a "$-$" is used for internal gears. Now, considering that both $b$ and $b_f$ represent the length of a meshing gear pair in one stage (i.e. $b_s$), Eq. (1) can be rewritten, such that the behaviour of the maximum allowable output torque can be calculated:

$$\begin{cases} T_{in,max} = \frac{\sigma_{H,ut}^2 d_1^2 b_s i_s}{2000 Z_E^2 Z_H^2 Z_\varepsilon^2 K_H (i_s \pm 1)} & \text{For contact stress} \\ \\ T_{in,max} = \frac{\sigma_{F,ut} d_1 b_s m}{2000 K_F Y_{FS} Y_\beta Y_\varepsilon} & \text{For bending stress} \end{cases} \tag{2}$$

To write these equations in an easier manner, each term needs to be investigated in order to see how they scale with volume.

Parameters, like $\sigma_H, \sigma_F, Z_E, Z_H, Z_\varepsilon, K_H, K_F$ and $Y_{FS}$ can be considered, for a given material and heat treatment, to be constant in a first approximation. Consequently, for the derivation of scaling laws, we can leave them out of the equation.

On the other hand, the transmission ratio cannot be left out, since it cannot be written that $i_s \approx (i_s \pm 1)$. This is due to the fact that the ratios for parallel shaft spur gears are not high enough. Theoretically this ratio is limited to $1:12.5$ [11], however the practical limit is $1:5$. Maxon is even stricter: transmission ratios only vary from $1:2.2$ to $1:3.6$ in each stage [15].

To see the possible output torque, the given input torque needs to be transformed. Since the meshing efficiency for spur gears is very high, the following approximation can be made:

$$T_{in,max} \cdot i_s = T_{out,max} \tag{3}$$

Also the gear module, which is written in the equation of bending stress, needs to be rewritten. The gear module is a parameter that indicates the size of the gear teeth. It is related to the pitch diameter of the gear as follows:

$$m = \frac{d_1}{z_1} = \frac{d_2}{z_2} \tag{4}$$

Inserting (3) and (4) into Eq. (2) gives:

$$\begin{cases} T_{out,max} \propto \frac{d_1^2 b_s i_s^2}{i_s \pm 1} & \text{For contact stress} \\ \\ T_{out,max} \propto d_1^2 b_s i_s & \text{For bending stress} \end{cases} \tag{5}$$

Both of the laws displayed in Eq. (5) are proportional with $d_1^2 b_s$, combined with a factor that contains transmission ratios. However, the inclusion of this factor will only give a spread on the data. We are on the other hand only interested in the maximum achievable torque, which will be achieved for a certain stage ratio. Other ones will lead to scaling lines with a lower maximum achievable torque Hence, to facilitate the scaling law, this factor can be neglected. Because of this, both contact stress and bending stress will lead to the same conclusion, namely:

$$T_{out,max} \propto b_s d_1^2 \tag{6}$$

Now, for a PSGT, the outer diameter of the gearbox is related to the pitch diameters of the individual gears as follows:

$$d \propto d_1 + d_2 \tag{7}$$

Combining this with the fact that it can be assumed that each stage has an equal width, i.e. $b_s = \frac{L}{a}$, where $a$ is the number of stages. The scaling law for the maximum achievable output torque becomes:

$$T_{out,max}^{PSGT} \propto \frac{L \cdot d^2}{a} \tag{8}$$

Hence, the torque is now represented by a volume divided by the number of stages. So for a same volume the torque capacity will lower if the number of stages increases. This seems to be logical, since the amount of material that remains for each stage decreases and hence each part is stressed more and the torque capacity is reduced.

Fig. 2 shows a plot with catalog data of gearboxes from Maxon in order to validate the scaling law in Eq. (8). In that figure an orange line can be observed which gives the optimal design solution according to the proposed scaling laws. The slope of this line is made using the derived law. Here, the intercept was made to match the points that achieved the maximum possible torque for an x-axis value.

This was done in such a way, since only the law for the maximum was calculated. Some points can also be below the line because their design is suboptimal in terms of strength, since a higher safety factor is taken and because the effect of the transmission ratios is neglected as scaling factor.

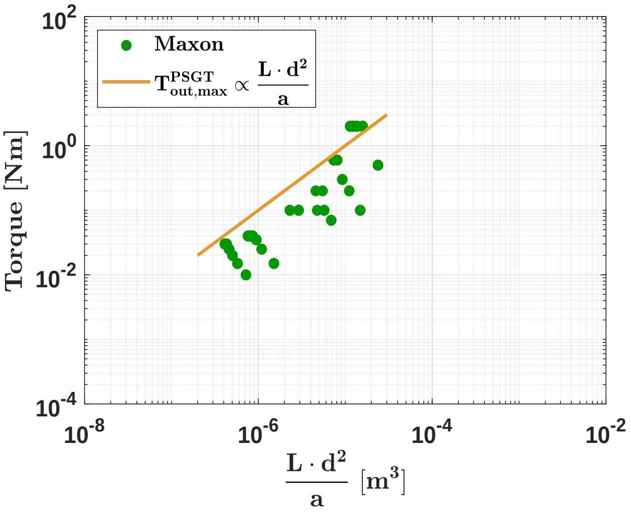

Fig. 2: Visualisation of the maximum continuous output torque of a multi-stage parallel shaft gear train (PSGT). The data is extracted from the catalogs of Maxon [15] , which is displayed in green. An orange trend line is plotted on these datapoints to show how the maximum achievable torque scales for each dimensional value.

### 2) *Total reflected inertia to the load side:*

For the dynamic character of a drive train, it is important to account for the reflected inertia of the drive train. This is important, since a low reflected inertia is the key to high-bandwidth actuation. Moreover, it lowers the impedance of the drive train, which is important when the actuator interacts with its environment [19].

In this subsection the reflected inertia of a PSGT transmission will be derived [20]. All inertia calculations in this paper will be reflected to the load side.

To determine $J_{PSGT}$, we will first look in one stage (i.e. $J_{PSGT,s}$):

$$J_{PSGT,s} = J_1 \cdot \left(\frac{\omega_1}{\omega_2}\right)^2 + J_2 = J_1 \cdot i_s^2 + J_2 \tag{9}$$

Now we only need to express $J_1$ and $J_2$ (inertia for respectively the pinion and gear) as functions of known variables. The mass moment of inertia of a cylinder around its axis of rotation is given by:

$$J_{cylinder} = \frac{\rho \pi h (d_{out} - d_{in})^4}{32} \tag{10}$$

Where $h$ is the length (height) of the cylinder, $\rho$ is the density, $d_{out}$ is the outer diameter and $d_{in}$ is the inner diameter. Thus, combining Eq. (9) and (10), leads to:

$$J_{PSGT,s} = \frac{\rho \pi b_s}{2} \cdot \left[\left(\frac{d_1}{2}\right)^4 \cdot i_s^2 + \left(\frac{d_2}{2}\right)^4\right] \tag{11}$$

Now still $d_1$ and $d_2$ need to be filled in. Combining Eq. (7) with the fact that $i_s = \frac{d_2}{d_1}$, it can be written that:

$$\begin{cases} d_1 \propto \frac{d}{1+i_s} \\ d_2 \propto \frac{d \cdot i_s}{1+i_s} \end{cases} \tag{12}$$

Implementing this in Eq. (11), gives:

$$J_{PSGT,s} \propto (\rho \pi b_s) \cdot \left(\frac{d}{2(1+i_s)}\right)^4 \cdot i_s^2 \tag{13}$$

When extending this to multiple stages, it should be taken into account that each stage adds another multiplication with the transmission ratio squared. Hence, when it is assumed that each stage uses the same configuration, the reflected mass moment of inertia of a PSGT is proportional to:

$$J_{PSGT} \propto J_{PSGT,s} \cdot \left(\sum_{k=0}^{a} i_s^{2k}\right) \tag{14}$$

Applying this, making the assumption that each stage has an equal length (i.e. $b_s = \frac{L}{a}$) and that $d_r \propto d$, the transmission inertia is given by:

$$J_{PSGT} \propto \frac{L \cdot d^4}{a} \cdot \left(\frac{i_s^2}{(1+i_s)^4}\right) \cdot \left(\sum_{k=0}^{a} i_s^{2k}\right) \tag{15}$$

Due to the influence of the transmission ratio, the effect of each stage increases the further it is away from the output. Hence, the total reflected inertia seen from the load side will be mainly determined by the input stage. However, since the other stages still also have an influence, the following assumption will be taken:

$$\left(\frac{i_s^2}{(1+i_s)^4}\right)\cdot\left(\sum_{k=0}^{a} i_s^{2k}\right)\approx C\cdot i_s^{2a} \tag{16}$$

Where $C$ is a constant. This is assumption is valid, because after verification it is seen that $C\in[0.03;0.057]$ for the range of possible transmission ratios. This shows that there is not even a factor 2 between the minimal and maximal value.

Applying (16) into Eq. (15), knowing that $i_s \approx \sqrt[a]{i}$, it can be written that the reflected inertia is given by:

$$J_{PSGT}\propto\frac{L\cdot d^4\cdot i^2}{a} \tag{17}$$

In Fig. 3 it can be seen that the derived law (orange line) follows the trend in gearbox inertia, based on catalog data from Maxon. Here, the intercept of this law was done in such a way that the line visually agrees with most of the data.

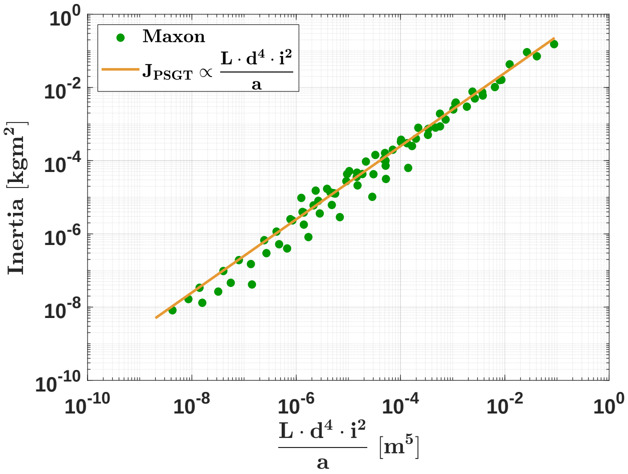

Fig. 3: Visualisation of the scaling of the inertia of a parallel shaft gearbox. The data is extracted from the catalogs of Maxon [15] (in green). An orange trend line is plotted on these data points to show how the transmission inertia scales for each dimensional value.

### B. Planetary Gear Train (PGT)

In this subsection, the previous equations and derivations will be interpreted for planetary gear trains. The parameters used here, which are specific to the PGT, can be seen in Table IV.

#### 1) Maximum Torque:

Compared to parallel shaft gears, the derivations for PGTs follow a similar process, although Eq. (1) should be treated with care. Since now there are two meshings, sun-planet and planet-ring, for each stage we should first look which one of the two is more restrictive to the output torque. Now, since $F_t = 2000\frac{T_{in}}{d_1}$ Eq. (1) can be written as:

| Symbol | Explanation | Unit |
|---|---|---|
| $d_s$ | Pitch diameter sun gear | $m$ |
| $d_r$ | Pitch diameter ring gear | $m$ |
| $d_p$ | Pitch diameter planet gear | $m$ |
| $F_s$ | Force on the sun gear | $N$ |
| $F_c$ | Force on the carrier | $N$ |
| $F_r$ | Force on the ring gear | $N$ |
| $F_t$ | Tangential force | $N$ |
| $\omega_s$ | Rotational speed of the sun gear | $\frac{rad}{s}$ |
| $\omega_c$ | Rotational speed of the carrier | $\frac{rad}{s}$ |
| $i_s$ | Transmission ratio in one stage ($=\frac{\omega_{in}}{\omega_{out}}=\frac{\omega_s}{\omega_c}$) | / |
| $J_{PGT}$ | Planetary gear inertia | $kgm^2$ |
| $b$ | Effective teeth width | $m$ |
| $b_s$ | Effective teeth width in one stage | $m$ |
| $b_f$ | Effective gear face | $m$ |

TABLE IV: Nomenclature of PGT specific parameters

$$\sigma_H = Z_E Z_H Z_\varepsilon\sqrt{\frac{K_H F_t(i_s\pm 1)}{b_2 d_1 i_s}} \tag{18}$$

In the most common planetary gear configuration, the sun (input) is driving the planet gears connected to a carrier (output) while the ring gear is grounded, as can be seen in Fig. 4.

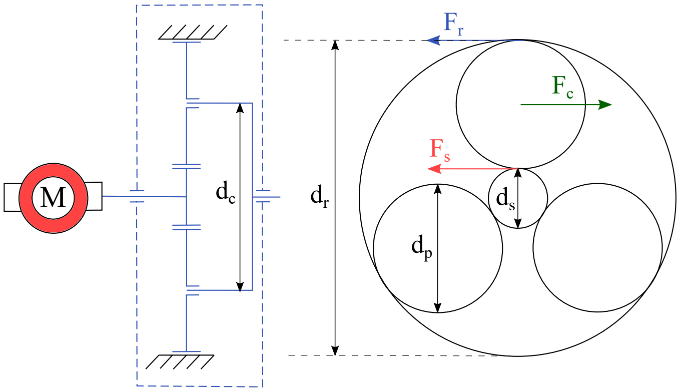

Fig. 4: Overview of the structure of one stage of a planetary gearbox together with the forces acting in this stage on a planet gear.

In order to find the meshing with the highest stress, the tangential forces acting on the planet due to the sun gear ($F_s$) and ring gear ($F_r$), which can be seen in Fig. 4, should be expressed as a function of the output torque ($T_{out}$). This can be done by expressing static equilibrium of the planet gear, and hence the following relation can be found:

$$|F_s| = |F_r| = \frac{|F_c|}{2} = \left|\frac{T_{out}}{d_s+d_p}\right| \tag{19}$$

Knowing this, the term $F_t$ in Eq. (18), can be replaced by Eq. (19). Hence, the expression for the maximum contact stress in the gears, for respectively the ring-planet interface and the sun-planet interface, becomes:

$$\begin{cases} \sigma_{H,max,pr} = Z'\sqrt{\frac{T_{out}}{d_s+d_p}\frac{\frac{d_r}{d_p}-1}{b_s d_r}} \\ \sigma_{H,max,sp} = Z'\sqrt{\frac{T_{out}}{d_s+d_p}\frac{\frac{d_p}{d_s}+1}{b_s d_p}} \end{cases} \tag{20}$$

Where $Z' = Z_E Z_H Z_\varepsilon \sqrt{K_H}$.

It can also be noted that $d_r > d_p$ for each configuration, which means that the square root will always be real.

However, the individual diameters of the different gears are not provided in the catalog of the manufacturers. In order to find the scaling of torque in PGTs, a closer look into their layout will allow us to find an expression for equation (20). For this particular PGT configuration the gear ratio, for one stage $i_s \approx \sqrt[a]{i}$, is equal to:

$$i_s = 2\left(\frac{d_p}{d_s}+1\right) \tag{21}$$

In this equation it can be seen that $i_s$ has a practical lower limit (i.e. $i_s > 2$). Furthermore, we can derive the following relation from Fig. 4:

$$d_r = d_s + 2d_p \tag{22}$$

Inserting equations (21) and (22) into (20), we obtain:

$$\begin{cases} \sigma_{H,max,pr} = Z'\sqrt{\frac{2T_{out}(i_s-1)}{b_s d_r^2 (i_s-2)}} \\ \sigma_{H,max,sp} = Z'\sqrt{\frac{2T_{out}(i_s-1)^2}{b_s d_r^2 (i_s-2)}} \end{cases} \tag{23}$$

By filling in the maximum allowable stress for the used material, the maximum output torque becomes:

$$\begin{cases} T_{out,max,pr} = \left(\frac{\sigma_{H,max,allowable}}{Z'}\right)^2 \cdot \left(\frac{(i_s-2)}{2\cdot(i_s-1)}\right) \cdot d_r^2 b_s \\ T_{out,max,sp} = \left(\frac{\sigma_{H,max,allowable}}{Z'}\right)^2 \cdot \left(\frac{(i_s-2)}{2(i_s-1)^2}\right) \cdot d_r^2 b_s \end{cases} \tag{24}$$

Here, it can be seen that the output torque will always be limited by the meshing between the sun and planet gear [21], since $i_s > 2$ for each configuration (as mentioned before). Hence, the scaling law for the torque, based on the contact stress, is approximated by:

$$T_{out,max} \propto \left(\frac{(i_s-2)}{(i_s-1)^2}\right) \cdot d_r^2 b_s \tag{25}$$

For multi-stage gearboxes the same scaling can be applied, since only the last stage will determine how much torque the entire gearbox can handle. Hence, by assuming that $d_r \propto d$ in combination with the fact that equal width is assumed for each stage, i.e. $b_s = \frac{L}{a}$, the scaling law becomes:

$$T_{out,max} \propto \frac{L \cdot d^2}{a} \cdot \frac{(i_s-2)}{(i_s-1)^2} \approx \frac{L \cdot d^2 \cdot (\sqrt[a]{i}-2)}{a(\sqrt[a]{i}-1)^2} \tag{26}$$

Including the number of stages ($a$) in this scaling is interesting, especially for efficiency purposes, since the more stages, the lower the energy efficiency. This law can be simplified into:

$$T_{out,max}^{PGT} \propto \frac{L \cdot d^2}{a} \tag{27}$$

In this equation the influence of the transmission ratio is left out. By doing this, the maximum torque line can still be seen for configurations with minimal stage ratios. Configurations with higher ratios will lead to lines that are parallel to the maximum achievable torque line as can be seen in Fig. 5.

This figure shows a plot with catalog data of gearboxes from Maxon, Moog and Neugart in order to validate the scaling law in Eq. (27). An orange line can be observed which gives the optimal design solution according to the proposed scaling laws. Note that some points are not only below the line because of the higher stage ratios that are used, but also because their design is suboptimal in terms of strength, since a higher safety factor is taken.

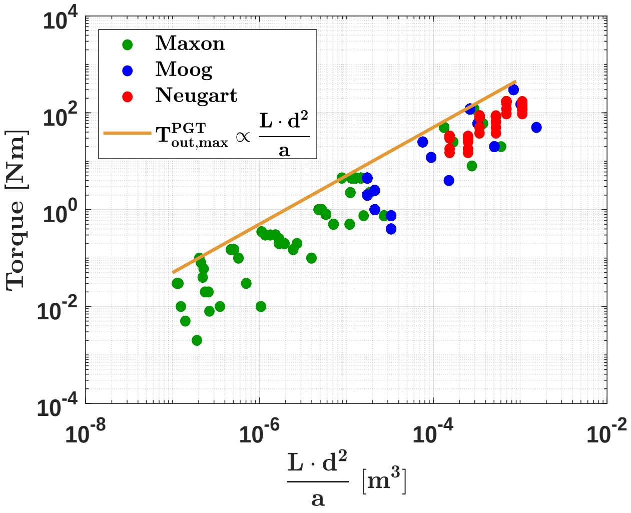

Fig. 5: Visualisation of the maximum continuous output torque of a planetary gearbox. The data is extracted from the catalogs of Maxon [15] (in green), Moog [16] (in blue), and Neugart [17] (in red). An orange trend line is plotted on these datapoints to show how the maximum achievable torque scales for each dimensional value.

### 2) *Total reflected inertia to the load side:*

To determine the reflected moment of inertia of a $PGT$, $J_{PGT}$, we will first look in one stage (i.e. $J_{PGT,s}$):

$$J_{PGT,s} = J_s \cdot \left(\frac{\omega_s}{\omega_c}\right)^2 + J_c + 3J_p \cdot \left(\frac{\omega_p}{\omega_c}\right)^2 \tag{28}$$

Combining Eqs. (10) and (28), applying either the graphical Kutzbach method [22] or the analytical Willis equation [23], it can be written that:

$$J_{PGT,s} = \frac{\rho \pi b_s}{32} \cdot \left[ d_s^4 \cdot i_s^2 + d_c^4 + 3d_p^4 \cdot \left( \frac{i_s}{i_s - 2} \right)^2 \right] \tag{29}$$

Furthermore, from Eqs. (21) and (22) and after some small geometric calculations, we find following expressions for the diameter of the sun, planets and carrier:

$$\begin{cases} d_s & = \frac{d_r}{i_s - 1} \\ d_p & = \frac{d_r \cdot (i_s - 2)}{2(i_s - 1)} \\ d_c & = \frac{d_r \cdot i_s}{2(i_s - 1)} \end{cases} \tag{30}$$

Implementing (30) in (29), gives that:

$$J_{PGT,s} = \frac{\rho \pi b_s d_r^4 i_s^2}{128(i_s - 1)^4} \cdot \left( i_s^2 - 3i_s + 7 \right) \tag{31}$$

To extend these equations to multiple stages, the same method can be applied as for the spur gears. Assuming again that $b_s = \frac{L}{a}$ and that $d_r \propto d$, the total reflected mass moment of inertia of the *PGT* can be written as:

$$J_{PGT} \propto \frac{L \cdot d^4}{a} \cdot \left( \frac{i_s^2 \cdot (i_s^2 - 3i_s + 7)}{(i_s - 1)^4} \right) \cdot \left( \sum_{k=0}^{a} i_s^{2k} \right) \tag{32}$$

Now again, similar to what was done for the PSGTs, the terms that contain the stage ratios are approximated by their highest term (i.e. the first stage after the motor). Thus the approximation is made that:

$$\left( \frac{i_s^2 \cdot (i_s^2 - 3i_s + 7)}{(i_s - 1)^4} \right) \cdot \left( \sum_{k=0}^{a} i_s^{2k} \right) \approx C \cdot i_s^{2a} \tag{33}$$

Also here the assumption can be made, cause after verification it is seen that $C \in [1.185; 1.73]$ for the range of possible transmission ratios. This range is even smaller than for the PSGT.

Applying (33) into Eq. (32), knowing that $i_s \approx \sqrt[a]{i}$, it can be written that the reflected inertia is given by:

$$J_{PGT} \propto \frac{L \cdot d^4 \cdot i^2}{a} \tag{34}$$

In Fig. 6 it can be seen that the orange line, which represents the derived law (i.e. Eq. (34)), follows rather accurately the inertia values of different gearboxes, which are extracted from the catalogs of Maxon, Moog and Neugart.

## III. SCALING FOR HARMONIC DRIVES (HD)

In this section, calculations are made regarding harmonic drives (HDs). The parameters involved in these calculations are summarized in TABLE V.

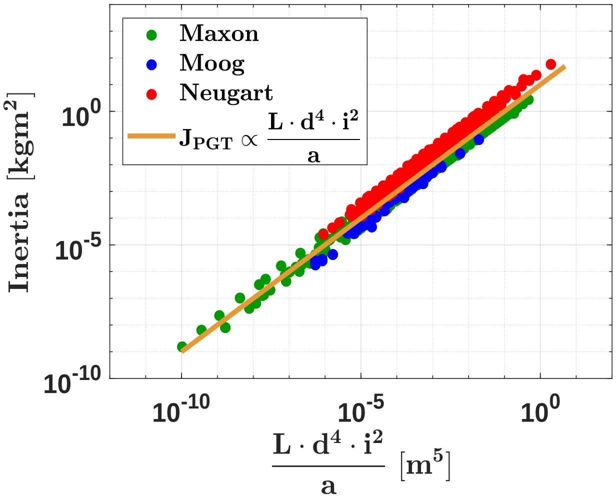

Fig. 6: Visualisation of the scaling of the inertia of a planetary gearbox. The data is extracted from the catalogs of Maxon [15] (in green), Moog [16] (in blue) and Neugart [17] (in red). An orange trend line is plotted on these data points to show how the transmission inertia scales for each dimensional value.

| Symbol | Explanation | Unit |
|---|---|---|
| $h_{ml}$ | Rim tooth thickness flexspline | $m$ |
| $d_f$ | Pitch diameter of the flexspline | $m$ |
| $\sigma_{F0}$ | Endurance limit | $\frac{N}{m^2}$ |
| $i$ | Transmission ratio of the harmonic drive ($=\frac{\omega_{in}}{\omega_{out}}$) | / |
| $d$ | Outer diameter of the harmonic drive | $m$ |
| $L$ | Length of the harmonic drive | $(m)$ |
| $T_{out,max}$ | Maximum allowable continuous output torque | $Nm$ |
| $J_{HD}$ | Mass moment of inertia of the harmonic drive | $kgm^2$ |
| $J_{WG}$ | Mass moment of inertia of the wave generator | $kgm^2$ |
| $J_{FS}$ | Mass moment of inertia of the flexspline | $kgm^2$ |
| $J_{CS}$ | Mass moment of inertia of the circular spline | $kgm^2$ |
| $\omega_{WG}$ | Rotational speed of the wave generator | $\frac{rad}{s}$ |
| $\omega_{FS}$ | Rotational speed of the flexspline | $\frac{rad}{s}$ |
| $\omega_{CS}$ | Rotational speed of the circular spline | $\frac{rad}{s}$ |

TABLE V: Nomenclature of harmonic drives

### A. *Stress Calculations*

#### 1) *Maximum Torque:*

Harmonic drives, which can be seen in Fig. 7, consist of three parts:

- Elliptical wave generator (WG)
- Flexspline (FS)
- Circular spline (CS)

In harmonic drives, the wave generator is generally used as input. It is a cam with an elliptical shape which is fitted into a bearing. This wave generator is then mounted inside a flexible hub (the flexspline). The flexspline has an outer gearing which is pressed into rigid circular spline, which has internal gearing and is usually grounded. Due to the fact that the flexspline is

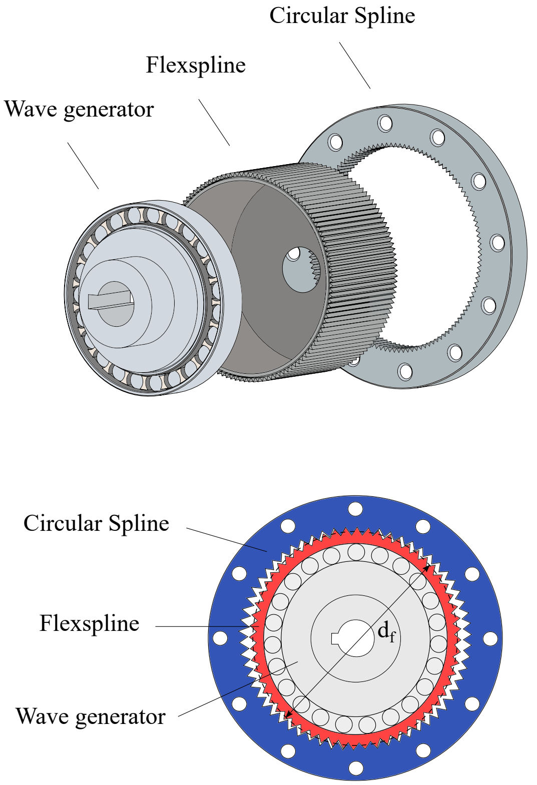

Fig. 7: Exploded view of the different parts of a harmonic drive (top) and a detailed cross-section view of it (bottom).

flexible it has a higher loading capacity, since up to 30% of the teeth are constantly in contact [24].

However, it is constantly subjected to deformation. These periodic deformations make that the flexspline is the weakest part of a harmonic drive and hence will determine its torque capacity [25], [26]. Due to the periodic nature of the deformation, the main failure mechanism is fatigue. Because of this, the endurance limit ($\sigma_{F0}$), and not the tensile or yield strength will be used in the calculation of the maximum allowable output torque. The endurance limit is a fatigue parameter that defines the maximum amount of cycles a material can withstand under bending stress, without experiencing failure due to fatigue.

According to [27], the relationship between the maximum output torque and the endurance limit is given by:

$$h_{ml} = \left( \frac{10600 \cdot T_{out,max}}{\sigma_{F0} \cdot d_f^3} + 7 \cdot 10^{-3} \right) \cdot d_f \tag{35}$$

Hence, the maximum allowable output torque is given by:

$$T_{out,max} = \frac{\sigma_{F0} \cdot d_f^2}{10600} \cdot \left( h_{ml} - 7 \cdot 10^{-3} \cdot d_f \right) \tag{36}$$

It is also indicated in [27] that $h_{ml}$ has a maximum allowable value of $0.018 d_f$. This indicates that there is a relationship between $h_{ml}$ and $d_f$, since manufacturers usually try to maximize torque. By implementing this assumption in Eq. (36), the output torque (and more specifically the maximum continuous output torque if it is assumed that $\sigma_{F0}$ reaches the value of $\sigma_{max}$) scales like:

$$T_{out,max} \propto d_f^3 \tag{37}$$

Because the flexspline is the largest part of the HD, it is reasonable to assume that the pitch diameter of the flexspline, i.e. $d_f$, is proportional to the output diameter $d$ of the harmonic drive. Eq. (37) can thus be simplified to:

$$T_{out,max}^{HD} \propto d^3 \tag{38}$$

When comparing this formula to catalog data from Harmonic Drive® [28], see Fig. 8, it can be seen that this trend is indeed visible.

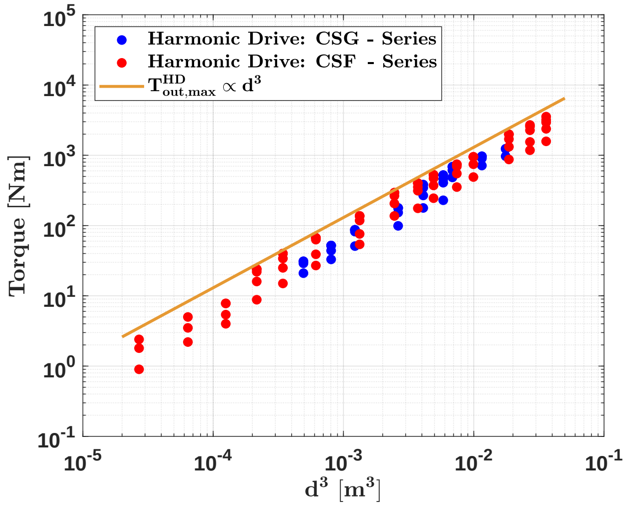

Fig. 8: Visualisation of the maximum continuous output torque of a harmonic drive. The data is extracted from the catalogs of Harmonic Drive® [28] for both the CSG-series (in blue), and the CSF-series (in red). An orange trend line is plotted on these data points to show how the maximum continuous output torque scales for each dimensional value.

### 2) *Total reflected inertia to the load side:*

In this subsection, the total reflected mass moment of inertia of a harmonic drive will be derived looking from the load side. In its most general form, the total moment of inertia of the harmonic drive, $J_{HD}$, can be written as:

$$J_{HD} = \left( \frac{\omega_{WG}}{\omega_{out}} \right)^2 \cdot J_{WG} + \left( \frac{\omega_{FS}}{\omega_{out}} \right)^2 \cdot J_{FS} + \left( \frac{\omega_{CS}}{\omega_{out}} \right)^2 \cdot J_{CS} \tag{39}$$

Since usually the wave generator is used as input, the flexspline as output and the circular spline as fixed element, Eq. (39) can be rewritten as:

$$J_{HD} = i^2 \cdot J_{WG} + J_{FS} \tag{40}$$

All these parts can be approximated as cylinders. Now, when looking to Eq. (10), it can be seen that $d_{out} \approx d_{in}$, since the flexspline is very thin. Due to this, in combination with the fact that the inertia of the flexspline does not need to be transformed to the outside, the assumption can be made that the influence of the flexspline inertia is negligible in the total reflected inertia.

Hence, we can apply Eq. (10), where again $h$ is assumed to be proportional to the outer length $L$ and $d_{out}$ is assumed to be proportional to the outer diameter of the harmonic drive $d$. Consequently, the total reflected moment of inertia seen from the load side is given by:

$$J_{HD} \propto L \cdot d^4 \cdot i^2 \tag{41}$$

Comparing Eq. (41) to catalog data from Harmonic Drive® [28], see Fig. 9, it can be seen that this trend is indeed visible.

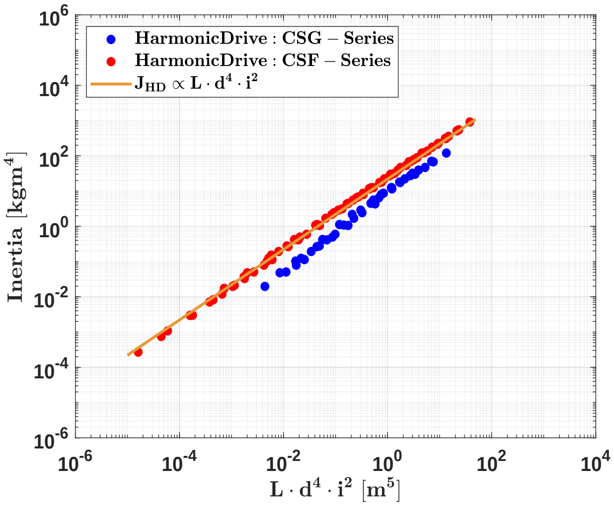

Fig. 9: Visualisation of the reflected inertia of a harmonic drive. The data is extracted from the catalogs of Harmonic Drive® [28] for both the CSG-series (in blue), and the CSF-series (in red). An orange trend line is plotted on these data points to show how the reflected inertia scales for each dimensional value.

## IV. SCALING FOR CYCLOID DRIVES (CYCLO)

In this section, calculations are made regarding cycloid drives. The parameters involved in these calculations are summarized in TABLE VI.

### A. Stress Calculations

#### 1) Maximum Torque:

Cycloid drives, which can be seen in Fig. 10, consist of four parts:

- Input shaft with eccentric cam (EC)
- Cycloid disc (CD)
- Ring rollers with ring gear (RR)
- Output disc (OD)

| Symbol | Explanation | Unit |
|---|---|---|
| $\sigma_{F,max}$ | Maximum allowable bending stress | $\frac{N}{m^2}$ |
| $M$ | Bending moment on the output pins | $Nm$ |
| $c$ | Distance from the neutral fiber to the point of max. stress | $m$ |
| $I$ | Area moment of inertia of the cross-section | $m^4$ |
| $F_s$ | Force acting between cycloid disc and output pins | $N$ |
| $x$ | Lever arm from output disc to where force is applied | $m$ |
| $d'_p$ | Diameter of the output pins | $m$ |
| $d_p$ | Diameter of the output rollers | $m$ |
| $d_h$ | Diameter of output holes | $m$ |
| $t$ | Thickness of the cycloid disc | $m$ |
| $r_w$ | Radius of roller pin circle | $m$ |
| $r_2$ | Radius of output pin circle | $m$ |
| $z_w$ | Number of output holes | / |
| $e$ | Eccentricity of the input cam | $m$ |
| $m$ | Gear module | $m$ |
| $i$ | Transmission ratio of the cycloid drive ($=\frac{\omega_{in}}{\omega_{out}}$) | / |
| $d$ | Outer diameter of the harmonic drive | $m$ |
| $L$ | Length of the harmonic drive | $m$ |
| $T_{out,max}$ | Maximum allowable continuous output torque | $Nm$ |
| $J_{Cyclo}$ | Mass moment of inertia of the cycloid drive | $kgm^2$ |
| $J_{shaft,in}$ | Mass moment of inertia of the input shaft | $kgm^2$ |
| $J_{BB}$ | Mass moment of inertia of the ball bearing | $kg$ |
| $J_{cam}$ | Mass moment of inertia of the wave generator | $kgm^2$ |
| $J_{CD}$ | Mass moment of inertia of the cycloid disc | $kgm^2$ |
| $J_{OD}$ | Mass moment of inertia of the output disc | $kgm^2$ |
| $m_{cam}$ | Mass of the eccentric cam | $kg$ |
| $m_{BB}$ | Mass of the ball bearing | $kg$ |
| $m_{CD}$ | Mass of the cycloid disc | $kg$ |
| $\omega_{EC}$ | Rotational speed of the eccentric cam with input shaft | $\frac{rad}{s}$ |
| $\omega_{CD}$ | Rotational speed of the cycloid disc | $\frac{rad}{s}$ |
| $\omega_{RR}$ | Rotational speed of the ring gear and ring rollers | $\frac{rad}{s}$ |
| $\omega_{OD}$ | Rotational speed of the output disc | $\frac{rad}{s}$ |

TABLE VI: Nomenclature of Cycloid Drives

In cycloid drives, the eccentric cam, which is rigidly connected to the input shaft, is used as input. This cam induces a cycloid motion that lets the cycloid disc roll over the rollers, which are fixed inside a grounded ring. These rollers can be either free or fused to the ring [29]. The pins of the output disc are inserted into holes in the cycloid disc. As a result, the output disc moves in the opposite way as the cycloid disc during the eccentric movement.

Due to the fact that the lobes of the cycloid disc roll on the rollers, only compressive force is created [30]. This means that failure will happen either due to bending stress or contact stress, which is similar to the failure mode of the PSGT and PGT.

Of all parts of the cycloid drive, the output pins undergo the highest forces [31] and are therefore the most critical components. Consequently, their dimensioning will determine the scaling law. Since a cycloid drive is sensitive to misalignment, bending stresses will be more critical than contact stresses.

The maximum allowed bending stress in these pins can be calculated using the bending beam equations:

$$\sigma_{F,ut} = \frac{M \cdot c}{I} \tag{42}$$

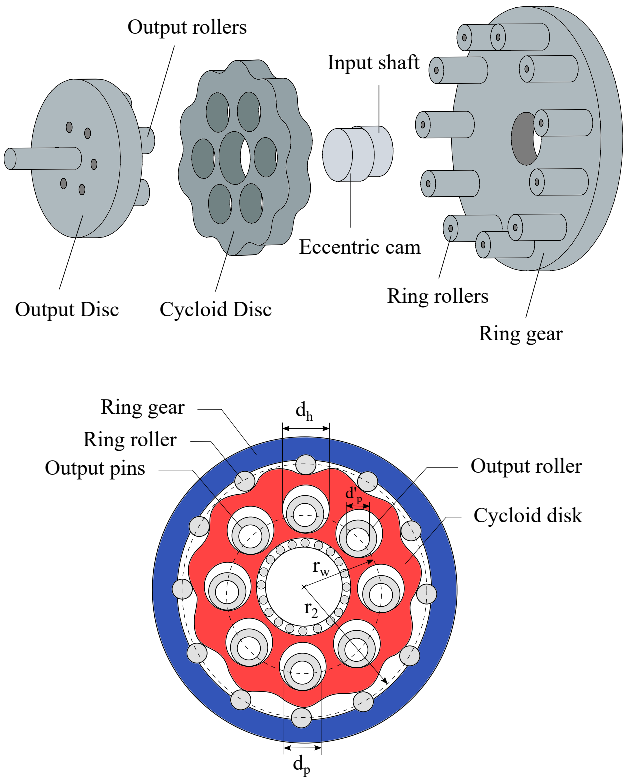

Fig. 10: Exploded view of the different parts of a cycloid drive (top) and a detailed cross-section view of the cycloid drive (bottom) together with all the parameters needed to describe it.

Referring to Fig. 10, these parameters can be written as:

$$\begin{cases} M & = F_s \cdot x \\ I & = \frac{\pi d_p'^4}{64} \\ c & = \frac{d_p'}{2} \end{cases} \tag{43}$$

According to [32], $F_s$ and $x$ are given by:

$$\begin{cases} F_s & = \frac{4.8 T_{out}}{z_w r_w} \\ x & = \frac{t}{2} \end{cases} \tag{44}$$

From substitution of Eqs. (43) and (44) into (42), it follows that the maximum allowed bending stress is given by:

$$\sigma_{F,ut} = \frac{76.8 T_{out} \cdot t}{\pi d_p'^3 \cdot z_w \cdot r_w} \tag{45}$$

In order to find a scaling law as a function of the outer parameters, i.e. length and diameter, the relation of each of the parameters in Eq. (45) with these outer parameters should be found.

The width of the cycloid disc ($t$) has to be the same as the one of static rollers, the same as the eccentric cam and approximately the same as the output pins. An increase of $t$ leads to proportional increase in the overall length, because other parts that define the length - the output disc and the shafts - adapt accordingly. Note that usually a double or triple cycloid disc is placed (all with the same thickness) for balancing purposes. Placing two or three cycloid discs however does not change the proportionality link with the total length $L$. Furthermore, the radial distance to the center of the output pins ($r_w$) can be related to an output parameter. According to [32], the ratio between the radial distance of the center of the output pins and that of the center of the ring rollers ($r_2$) is given by:

$$\frac{r_w}{r_2} = \frac{2e}{m} \tag{46}$$

Now, it can be assumed that the pitch radius is proportional to the outer diameter, since the outer ring is the only distance in between. It follows that also $r_w \propto d$.

For the last parameter, $d_p'$, it should first be noted that the diameter of the output pin and the output roller ($d_p$) are proportional [32]. There is also a linear relationship between the diameter of the output hole ($d_w$) and the diameter of the output roller. This relationship is given by [33]:

$$d_h = d_p + 2e \tag{47}$$

Referring to the bottom picture of Fig. 10, it can easily be seen that, for a given shaft, the outer diameter of the cycloid drive has to increase if the output hole increases. Hence, the assumption can be made that $d_w \propto d$.

In summary, it can be written that:

$$\begin{cases} d_p' & \propto d \\ r_w & \propto d \\ t & \propto L \end{cases} \tag{48}$$

Inserting (48) into Eq. (45), we find that the maximum allowable output torque of a cycloid drive scales as:

$$T_{out,max}^{Cyclo} \propto \frac{d^4}{L} \tag{49}$$

A comparison with catalog data from Sumitomo [34], shown in Fig. 11, confirms this trend.

### 2) *Total reflected inertia to the load side:*

In this subsection, the total reflected mass moment of inertia of a cycloid drive will be derived, looking from the load side. To determine $J_{Cyclo}$, we first start again with the most general form:

$$J_{cyclo} = \left(\frac{\omega_{EC}}{\omega_{out}}\right)^2 J_{EC} + \left(\frac{\omega_{CD}}{\omega_{out}}\right)^2 J_{CD} + \left(\frac{\omega_{RR}}{\omega_{out}}\right)^2 J_{RR} + \left(\frac{\omega_{OD}}{\omega_{out}}\right)^2 J_{OD} \tag{50}$$

Due to the eccentric cam, the center of mass of the input shaft and the eccentric cam with ball bearing does not coincide with the central axis of the harmonic drive. The parallel axis theorem ($J' = J + me^2$) must therefore be applied to calculate the moment of inertia of those parts. Combined with the fact that the ring gear and ring rollers are static, we find:

$$J_{Cyclo} = i^2 \left[J_{shaft,in} + J_{cam} + J_{BB} + J_{CD} + e^2 (m_{cam} + m_{BB} + m_{CD})\right] + J_{OD} \tag{51}$$

In this equation, the influence of the output disc can be neglected, since it is already turning at the output side and

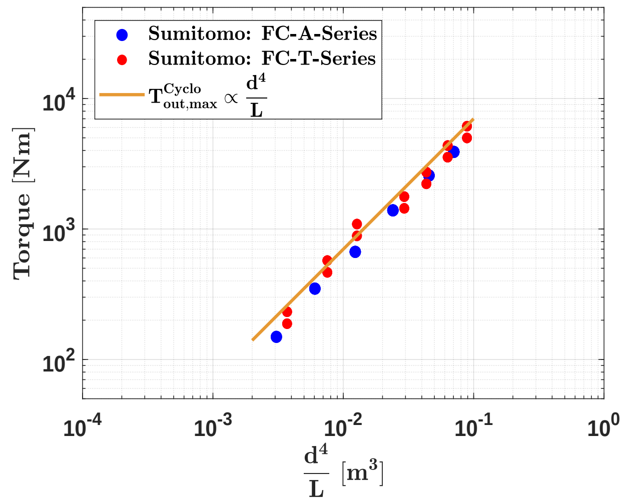

Fig. 11: Visualisation of the maximum continuous output torque of a cycloid drive. The data is extracted from the Fine Cyclo catalogs of Sumitomo [34] for both the A-series (in blue), and the T-series (in red). For the A-series, there are several different subseries based on the used bearing for the output flange, but here the standard variant is taken. An orange trend line is plotted on these data points to show how the maximum continuous output torque scales for each dimensional value.

hence has no influence from the transmission ratio, which makes its contribution to the reflected inertia very small in comparison to the other parts.

For the rest of the cycloid drive, all parts are (roughly) cylindrical, so it can be assumed that their masses also scale with $L \cdot d^2$. It can also be said that the eccentricity ($e$) depends on the available diameter. This combined with Eq. (10), assuming again that $h \propto L$ and $d_{out} \propto d$, gives:

$$J_{Cyclo} \propto L \cdot d^4 \cdot i^2 \tag{52}$$

Comparing Eq. (52) to catalog data from Sumitomo [34], see Fig. 12, it can be seen that this trend is indeed visible. Only the FA-series deviate slightly from this trend line, but this is due to the fact that they use a slightly different internal design. It can however be noted that this does not impose great changes to the predicted behaviour.

## V. SCALING FOR BALL SCREWS (BS)

In this section, calculations are made regarding ball screws (BS). These calculations are made according to the equations found in [35] and [36]. The parameters involved in these calculations are summarized in TABLE VII.

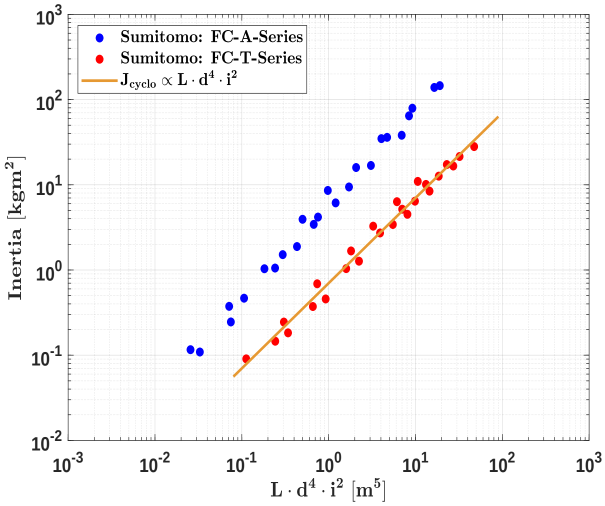

Fig. 12: Visualisation of the reflected inertia of a cycloid drive. The data is extracted from the Fine Cyclo catalogs of Sumitomo [34] for both the A-series (in blue), and the T-series (in red). For the A-series, there are several different subseries based on the used bearing for the output flange, but here the standard variant is taken. An orange trend line is plotted on these data points to show how the reflected inertia for each dimensional value.

| Symbol | Explanation | Unit |
|---|---|---|
| $F_L$ | Ball screw feed force | $N$ |
| $\sigma_{eq}$ | Equivalent stress of combined load | $\frac{N}{m^2}$ |
| $T$ | Ball screw torque | $Nm$ |
| $T_{max}$ | Maximum allowed ball screw torque | $Nm$ |
| $\eta$ | Ball screw efficiency | / |
| $d$ | Output diameter of the screw | $m$ |
| $d_r$ | Minor diameter of the screw | $m$ |
| $p$ | Thread lead of the screw | $m$ |
| $L$ | Length of the screw | $m$ |
| $m_{screw}$ | Screw mass | $kg$ |
| $m_{nut}$ | Nut mass | $kg$ |
| $n_t$ | Number of engaged threads | / |
| $l_{nut}$ | Length of the nut | $m$ |
| $J_{BS}$ | Mass moment of inertia of the complete ball screw | $kgm^2$ |
| $J_{screw}$ | Mass moment of inertia of the screw | $kgm^2$ |
| $J_{nut}$ | Mass moment of inertia of the nut | $kgm^2$ |

TABLE VII: Nomenclature of ball screws

### A. *Stress Calculations*

#### 1) *Maximum Torque:*

Ball screws, depicted in Fig. 13, are subject to different kinds of loads, which result in different types of stresses. The most prominent ones are:

- Maximum bending stress at root of the thread: $\sigma_b$
- Maximum bearing stress at the nut and screw: $\sigma_{br}$
- Maximum compressive stress in screw body: $\sigma_c$
- Maximum torsional shear stress: $\tau$

These stresses are given by:

$$\begin{cases} \sigma_c &= \frac{4F_L}{\pi d_r^2} \\ \tau &= \frac{16T}{\pi d_r^3} \\ \sigma_b &= \frac{6F_L}{\pi d_r n_t p} \\ \sigma_{br} &= \frac{3F_L}{\pi d_r l_{nut}} \end{cases} \tag{53}$$

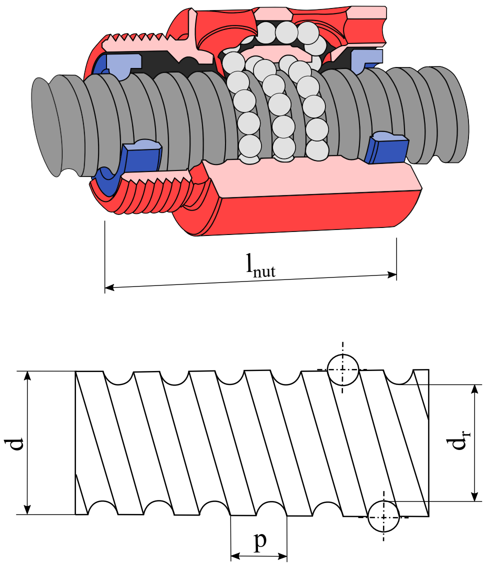

Fig. 13: Overview of the structure of a complete ball screw (top) and of the detailed view of the screw itself (bottom) together with all the parameters needed to describe it.

According to [37], the main failure mechanism in ball screws is fatigue in the screw due to the repeated compressive stress. This often leads to flaking, a fatigue fracture that causes the grooves of the screw to exfoliate due to the compressive stress. The surface of the screw is also subject to non-negligible shear stresses, which need to be taken into account.

From the above, it can be concluded that the first two stresses of (53), i.e. $\sigma_c$ and $\tau$, will be the limiting factor and hence will define the scaling law. The maximum allowed equivalent stress is calculated from the Von Mises stress criterion [36]:

$$\begin{aligned} \sigma_{eq} &= \sqrt{\sigma_c^2 + 3\tau^2} \\ &= \sqrt{\left(\frac{4F_L}{\pi d_r^2}\right)^2 + 3\left(\frac{16T}{\pi d_r^3}\right)^2} \end{aligned} \tag{54}$$

To transform the torque $T$ into the feed force $F_L$, the following equation can be used [15]:

$$T = \frac{pF_L}{2\pi\eta} \tag{55}$$

In this equation, the lead $p$ is defined as the axial distance travelled by the screw in one complete revolution of the shaft [38]. This distance, which is equal to the pitch for single-start screws, is dependent on the diameter of the screw. Because the pitch increases for screws with a higher diameter, so will the lead. So, to facilitate the derivation of Eq. (54), the following assumptions are made:

$$\begin{cases} d_r &\propto d \\ p &\propto d \end{cases} \tag{56}$$

If now Eq. (55) is implemented in Eq. (54), together with the above assumptions, the scaling law of the maximum continuous torque of a spindle can be found:

$$\begin{aligned} \sigma_{eq} &\propto \sqrt{\left(\frac{8\eta T}{d^3}\right)^2 + 3\left(\frac{16T}{\pi d^3}\right)^2} \\ &\propto \frac{T}{d^3} \cdot \sqrt{(8\eta)^2 + 3\left(\frac{16}{\pi}\right)^2} \end{aligned} \tag{57}$$

Replacing the equivalent stress $\sigma_{eq}$ by the maximum allowable stress of the screw material, it is found that the torque scales as:

$$T_{max} \propto \frac{d^3}{\sqrt{\eta^2 + \left(\frac{12}{\pi^2}\right)}} \tag{58}$$

Efficiencies of ball screws vary little among different sizes, with typical efficiencies around 90%. As a result, the denominator of (58) can be treated as a constant. Hence, the max. cont. torque will scale as:

$$T_{max}^{BS} \propto d^3 \tag{59}$$

Fig. 14 confirms this assumption, as the orange line according to Eq. (59) follows the trend in the plotted catalog data.

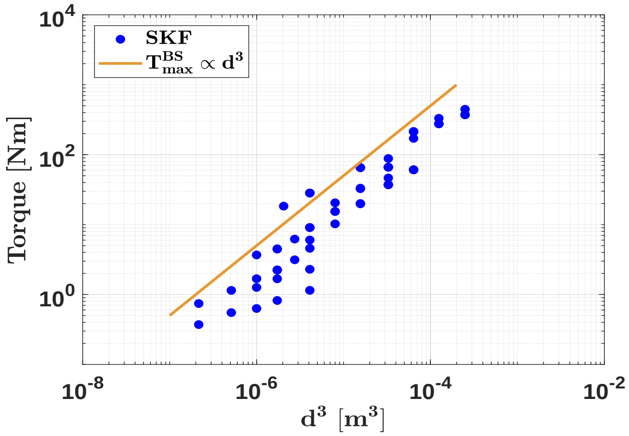

Fig. 14: Visualisation of the maximum continuous output torque of a ball screw, extracted from SKF [39] (in blue). An orange line is plotted on these datapoints to indicate the scaling of the maximum achievable torque for each dimensional value.

### 2) Total reflected inertia to the load side:

In this subsection, the total reflected mass moment of inertia of a ball screw will be derived. To determine $J_{BS}$, we can use the following formula [39]:

$$J_{BS} = J_{screw} + J_{nut} = \frac{m_{screw} \cdot d^2}{8} + m_{nut} \left(\frac{p}{2\pi}\right)^2 \qquad (60)$$

Due to the fact that the inertia of the screw is larger than the one of the nut (due to a large difference in size), the assumption can be made that $J_{nut}$ is negligible in comparison with $J_{screw}$. Combined with the fact that the mass of the screw scales with $d^2 \cdot L$, the mass moment of inertia of the ball screw scales as:

$$J_{BS} \propto L \cdot d^4 \qquad (61)$$

This behaviour can be seen in Fig. 15. In this figure the SKF catalog values of the ball screw inertia are plotted (in blue) as a function of the found scaling law. The scaling law nicely predicts the inertia, except for some points in the low dimensions. This is due to the fact that for small values of the screw, the relative value of $J_{nut}$ increases and cannot be neglected anymore. This is however only true for a limited range.

## VI. DISCUSSION

In this paper, the scaling laws of maximum continuous output torque and reflected inertia (to the load side) have been derived. A summary of these laws can be seen in Table VIII.

In this section, the found laws will be discussed based on the impact they have on the design of transmissions. Here also the different technologies will be compared among each other in an absolute way with the catalog data and the reflected inertia will be compared with the reflected inertia of commercial BLDC motors.

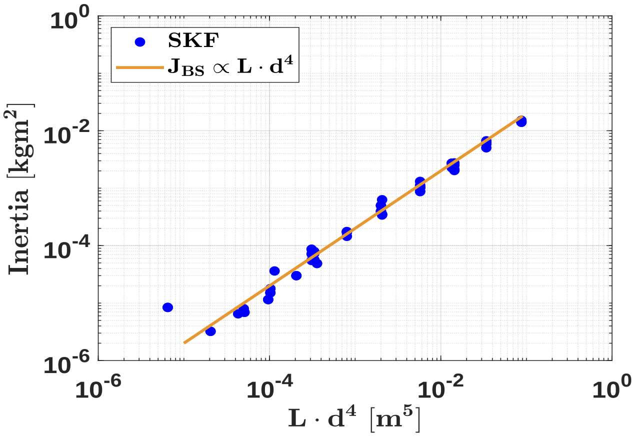

Fig. 15: Visualisation of the mass moment of inertia of a ball screw, extracted from SKF [39] (in blue). An orange line is plotted on these datapoints to indicate the scaling of the inertia for each dimensional value.

### A. Maximum continuous output torque

Looking at Table VIII, it can immediately be seen that there is a great dependency between the outer diameter of a transmission and the maximum continuous output torque it can withstand. This in contrast with the length, which appears to have a minimal or negative influence. For PGTs and PSGTs, an increase in length still contributes to a higher torque, but in the scaling laws for the harmonic drive and ball screw the length has no effect. For cycloid drives, an increase in length even has a negative impact on the maximum continuous output torque. This is most likely due to the fact that for longer cycloid drives, the lever arm of the output pins increases, which in return increases the bending stresses.

From the above, we can conclude that it is advisable for transmissions in robotics to be disc-shaped and not cylinder-

| | **Maximum continuous output torque** | **Reflected inertia (to load side)** |
|---|---|---|
| **Parallel Shaft Gear Train (PSGT)** | $\frac{L \cdot d^2}{a}$ | $\frac{L \cdot d^4 \cdot i^2}{a}$ |
| **Planetary Gear Train (PGT)** | $\frac{L \cdot d^2}{a}$ | $\frac{L \cdot d^4 \cdot i^2}{a}$ |
| **Harmonic Drive** | $d^3$ | $L \cdot d^4 \cdot i^2$ |
| **Cycloid Drive** | $\frac{d^4}{L}$ | $L \cdot d^4 \cdot i^2$ |
| **Ball Screw** | $d^3$ | $L \cdot d^4$ |

TABLE VIII: Overview of the scaling laws for maximum continuous output torque and reflected inertia (to load side) for different transmission types. These laws are made with the outer parameters of the transmission (i.e. diameter ($d$) and length ($L$), their transmission ratio ($i$) and number of stages ($a$).

shaped when high torque is desired.

### B. *Reflected inertia*

Looking at the reflected inertia it can again be said that the outer diameter has the largest influence, since all laws contain the factor $d^4$ while only $L^1$ for the length. In robotics, a small reflected inertia is often desirable because it allows the robot the react faster. Furthermore, reflected inertia is a crucial parameter in human-robot interaction. Here, the actuator's impedance - for a large part determined by reflected inertia - should be lowered as much as possible to guarantee safe interaction.

Now, since the torque and inertia have conflicting demands for the outer diameter of the transmission, it should be investigated whether the inertia of the transmission is relevant with respect to the one of the motor. To do so, the relative influence of the reflected motor inertia and transmission inertia for a motor-transmission couple should be compared against each other as a function of the allowed torque. Since it is not known with which transmission the motor is coupled, the total output torque and reflected inertia seen from the load side cannot be calculated for the motor. To solve this, the inertia will be given for both motor and reducer on the motor side. This will be as a function of the maximum allowable torque for the motor, and the maximum allowable input torque for the transmission. This data is depicted in Fig. 16, where two different BLDC motor constructions (Maxon EC-flat and Maxon EC [15]) are compared to the three most used reducers, i.e. a PGT, a harmonic drive and a cycloid drive.

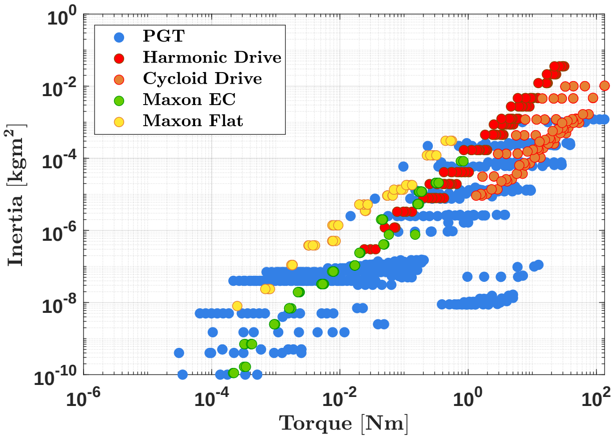

Fig. 16: Comparison between magnitude of motor inertia and transmission inertia, done for two different BLDC motor constructions (Maxon EC-flat and Maxon EC [15]) and three types of transmissions (a PGT, a harmonic drive and a cycloid drive). For these transmissions, the catalogs from Maxon [15], Moog [16], Neugart [17], Sumitomo [34] and Harmonic Drive [28] are used. Both inertia and torque are seen from motor side to provide a correct comparison.

From this figure, it can not only be concluded that harmonic drives have a rather high inertia in comparison with cycloid drives and PGTs, but also that the motor inertia will usually be higher (especially for Maxon EC-flat). It can also be noted that the spread of the PGT's inertia is very large, which is due to their broad range of possible constructions. This allows them to have options with rather low inertia as well.

Hence, for most configurations the motor inertia will be higher than the transmission inertia. In terms of design this can give some insight for the trade-off between high torque/low reflected inertia, since they have conflicting demands for the outer diameter. Due to the fact that it is less crucial to have a minimal output diameter, since its relevance for the total drive train inertia is usually lower than that of the motor, one can lean more into a design with an increased diameter.

## VII. CONCLUSION

In this paper, scaling laws are derived for parallel shaft gears, planetary gears, harmonic drives, cycloid drives and ball screws in function of their diameter, length, number of stages and transmission ratio. The proposed scaling laws for transmissions were shown to follow catalog in a satisfactory manner. The derived scaling laws show that from the two dimensional parameters (the length $L$ and the diameter $d$), the diameter has the most influence on torque and inertia. It was also found that in terms of torque optimization, a disc-shaped transmission is preferred over a cylinder-shaped one. The same cannot be said for inertia, since it has conflicting demands in terms of diameter selection. It was however shown that a minimal diameter for the inertia is not always crucial, since the inertia of the motor to which it is coupled, is usually more important for the overall drive-train inertia.

All these scaling laws can help to facilitate the design process, since the output characteristics can now be directly coupled to the dimensional parameters. This is especially relevant for complex actuators with multiple motors and gearboxes, such as the +SPEA [13] and DMA [14] developed in our group.

Because compliant elements are present in the +SPEA design, future work will first focus on the development of scaling laws for springs. Along with the known scaling laws for motors and the laws for gearboxes derived in this work, these will be used to optimize the design of these innovative actuators and assess their potential with respect to more conventional designs.

## ACKNOWLEDGMENT

Elias Saerens, Stein Crispel and Tom Verstraten are all affiliated with the Research Foundation Flanders. Elias Saerens and Stein Crispel as SB PhD Fellows and Tom Verstraten as a Postdoctoral Fellow. This work has been partially funded by the European Research Council Starting Grant SPEAR (grant no. 337596).

# REFERENCES

[1] Huber J. E., Fleck N. A., and Ashby M. F., “The selection of mechanical actuators based on performance indices,” *Proceedings of the Royal Society of London. Series A: Mathematical, Physical and Engineering Sciences*, vol. 453, no. 1965, pp. 2185–2205, Oct. 1997.

[2] A. J. Veale and S. Q. Xie, “Towards compliant and wearable robotic orthoses: A review of current and emerging actuator technologies,” *Medical Engineering & Physics*, vol. 38, no. 4, pp. 317–325, Apr. 2016.

[3] F. Casolo, S. Cinquemani, and M. Cocetta, “On active lower limb exoskeletons actuators,” in *2008 5th International Symposium on Mechatronics and Its Applications*, May 2008, pp. 1–6.

[4] I. W. Hunter, J. M. Hollerbach, and J. Ballantyne, “A comparative analysis of actuator technologies for robotics,” *Robotics Review*, vol. 2, pp. 299–342, 1991.

[5] T. Verstraten, G. Mathijssen, R. Furnémont, B. Vanderborght, and D. Lefeber, “Modeling and design of geared DC motors for energy efficiency: Comparison between theory and experiments,” *Mechatronics*, vol. 30, pp. 198–213, Sep. 2015.

[6] T. Verstraten, R. Furnémont, G. Mathijssen, B. Vanderborght, and D. Lefeber, “Energy Consumption of Geared DC Motors in Dynamic Applications: Comparing Modeling Approaches,” *IEEE Robotics and Automation Letters*, vol. 1, no. 1, pp. 524–530, Jan. 2016.

[7] S. Rezazadeh and J. W. Hurst, “On the optimal selection of motors and transmissions for electromechanical and robotic systems,” in *2014 IEEE/RSJ International Conference on Intelligent Robots and Systems*, Sep. 2014, pp. 4605–4611.

[8] H. L. Bartlett, B. E. Lawson, and M. Goldfarb, “On the design of power gear trains: Insight regarding number of stages and their respective ratios,” *PloS One*, vol. 13, no. 6, p. e0198048, 2018.

[9] A. Wang and S. Kim, “Directional efficiency in geared transmissions: Characterization of backdrivability towards improved proprioceptive control,” in *2015 IEEE International Conference on Robotics and Automation (ICRA)*, May 2015, pp. 1055–1062.

[10] P. P. Pott, “Entwurfskriterien feinwerktechnischer integrierter Sensor-Aktor-Systeme,” Apr. 2015.

[11] S. P. Radzevich, *Dudley’s Handbook of Practical Gear Design and Manufacture, Second Edition*, 2nd ed. Boca Raton, FL: CRC Press, May 2012.

[12] M. Budinger, J. Liscouët, F. Hospital, and J.-C. Maré, “Estimation models for the preliminary design of electromechanical actuators,” *Proceedings of the Institution of Mechanical Engineers, Part G: Journal of Aerospace Engineering*, vol. 226, no. 3, pp. 243–259, Mar. 2012.

[13] G. Mathijssen, R. Furnémont, T. Verstraten, B. Brackx, J. Premec, R. Jiménez, D. Lefeber, and B. Vanderborght, “+SPEA introduction: Drastic actuator energy requirement reduction by symbiosis of parallel motors, springs and locking mechanisms,” in *2016 IEEE International Conference on Robotics and Automation (ICRA)*, May 2016, pp. 676–681.

[14] T. Verstraten, R. Furnémont, P. López-García, D. Rodriguez-Cianca, H.-L. Cao, B. Vanderborght, and D. Lefeber, “Modeling and design of an energy-efficient dual-motor actuation unit with a planetary differential and holding brakes,” *Mechatronics*, vol. 49, pp. 134–148, Feb. 2018.

[15] *Motor Catalog Program 2017/18: High Precision Drives and Systems*. Maxon Motors A. G., 2018, [PDF file].

[16] *Motion Technology Catalog Brushless and Brush Motors, Drive Electronics, Gearheads and Position Sensors*. Moog Components Group, 2014, [PDF file].

[17] *Precision gearbox catalog*. Neugart GmbH, 2017, [PDF file].

[18] K.-H. Grote and E. K. Antonsson, Eds., *Springer Handbook of Mechanical Engineering*, ser. Springer Handbooks. Berlin Heidelberg: Springer-Verlag, 2009.

[19] N. Hogan, “Impedance Control: An Approach to Manipulation: Part ITheory,” *Journal of Dynamic Systems, Measurement, and Control*, vol. 107, no. 1, pp. 1–7, Mar. 1985.

[20] R. W. Armstrong, “Load to Motor Inertia Mismatch : Unveiling The Truth,” 1998.

[21] A. Terrin, C. Dengo, and G. Meneghetti, “Experimental analysis of contact fatigue damage in case hardened gears for off-highway axles,” *Engineering Failure Analysis*, vol. 76, pp. 10–26, 2017.

[22] K. Kutzbach, “Mechanische leitungsverzweigung, ihre gesetze und anwendungen,” *Maschinenbau*, vol. 8, no. 21, pp. 710–716, 1929.

[23] H. W. Müller, *Epicyclic Drive Trains: Analysis, Synthesis, and Applications*. Detroit: Wayne State University Press, Apr. 1982.

[24] H. S. Jeon and S. H. Oh, “A study on stress and vibration analysis of a steel and hybrid flexspline for harmonic drive,” *Composite Structures*, vol. 47, no. 1, pp. 827–833, Dec. 1999.

[25] J. Dai, L. Z. Chen, and X. B. Pang, “Design Optimization of the Flexspline in Harmonic Drive,” 2012.

[26] O. Kayabasi and F. Erzincanli, “Shape optimization of tooth profile of a flexspline for a harmonic drive by finite element modelling,” *Materials & Design*, vol. 28, no. 2, pp. 441–447, Jan. 2007.

[27] G. A. Timofeyev, Y. V. Kostikov, A. V. Yaminsky, and Y. O. Podchasov, “Theory and Practice of Harmonic Drive Mechanisms,” *IOP Conference Series: Materials Science and Engineering*, vol. 468, p. 012010, Dec. 2018.

[28] *CSF & CSG Series: Component Sets and Housed Units - catalog*. Harmonic Drive LLC, 2006, [PDF file].

[29] J. W. Sensinger, “Efficiency of High-Sensitivity Gear Trains, Such as Cycloid Drives,” *Transactions of the ASME, Journal of Mechanical Design*, vol. 135, no. 7, pp. 071 006/1–071 006/9, 2013.

[30] J. W. Sensinger and J. H. Lipsey, “Cycloid vs. harmonic drives for use in high ratio, single stage robotic transmissions,” in *2012 IEEE International Conference on Robotics and Automation*, May 2012, pp. 4130–4135.

[31] L. X. Xu, “A dynamic model to predict the number of pins to transmit load in a cycloidal reducer with assembling clearance,” *Proceedings of the Institution of Mechanical Engineers, Part C: Journal of Mechanical Engineering Science*, p. 0954406218809732, Nov. 2018.

[32] B. Borislavov, I. Borisov, and V. Panchev, “Design of a planetary-cyclo-drive speed reducer: cycloid stage, geometry, element analyses,” 2012.

[33] S. V. Thube and T. R. Bobak, “Dynamic Analysis of a Cycloidal Gearbox Using Finite Element Method,” 2012.

[34] *Fine Cyclo: Zero Backlash Speed Reducers - catalog*. Sumitomo Drive Technologies, 2011, [PDF file].

[35] J. E. . M. Shigley, Charles R., *Standard Handbook of Machine Design, 2 ed.* McGraw-Hill Professional, 1996.

[36] J. E. Shigley, *Mechanical Engineering Design*. McGraw-Hill, 1972.

[37] W. G. Lee, J. W. Lee, M. S. Hong, S.-H. Nam, Y. Jeon, and M. G. Lee, “Failure Diagnosis System for a Ball-Screw by Using Vibration Signals,” 2015.

[38] R. W. Burnham, *Mathematics for machinists*. New York, J. Wiley & sons, inc.; London, Chapman & Hall, limited, 1943.

[39] *Precision rolled ball screws - catalog*. SKF Group, 2013, [PDF file].

View publication stats